

Segmentation-Aware Generative Reinforcement Network (GRN) for Tissue Layer Segmentation in 3-D Ultrasound Images for Chronic Low-back Pain (cLBP) Assessment

Zixue Zeng, Xiaoyan Zhao, Matthew Cartier, Tong Yu, Jing Wang, Xin Meng, Zhiyu Sheng, Maryam Satarpour, John M Cormack, Allison Bean, Ryan Nussbaum, Maya Maurer, Emily Landis-Walkenhorst, Dinesh Kumbhare, Kang Kim, Ajay Wasan, Jiantao Pu

Abstract—We introduce a novel segmentation-aware joint training framework called generative reinforcement network (GRN) that integrates segmentation loss feedback to optimize both image generation and segmentation performance in a single stage. An image enhancement technique called segmentation-guided enhancement (SGE) is also developed, where the generator produces images tailored specifically for the segmentation model. Two variants of GRN were also developed, including GRN for sample-efficient learning (GRN-SEL) and GRN for semi-supervised learning (GRN-SSL). GRN's performance was evaluated using a dataset of 69 fully annotated 3D ultrasound scans from 29 subjects. The annotations included six anatomical structures: dermis, superficial fat, superficial fascial membrane (SFM), deep fat, deep fascial membrane (DFM), and muscle. Our results show that GRN-SEL with SGE reduces labeling efforts by up to 70% while achieving a 1.98% improvement in the Dice Similarity Coefficient (DSC) compared to models trained on fully labeled datasets. GRN-SEL alone reduces labeling efforts by 60%, GRN-SSL with SGE decreases labeling requirements by 70%, and GRN-SSL alone by 60%, all while maintaining performance comparable to fully supervised models. These findings suggest the effectiveness of the GRN framework in optimizing segmentation performance with significantly less labeled data, offering a scalable and efficient solution for ultrasound image analysis and reducing the burdens associated with data annotation.

Index Terms—Image Segmentation, Ultrasound Imaging, Chronic Lower Back Pain, Generative Adversarial Network.

I. INTRODUCTION

CHRONIC lower back pain (cLBP) is a complex and multifaceted condition [1]. It is highly prevalent, with 70-85% of individuals experiencing lower back pain (LBP) at some point in their lives [2]. Additionally, 19.6% of people aged between 20 and 59 report LBP [3], significantly affecting their quality of life [4]. Despite extensive research, etiology-based diagnosis and successful management of cLBP remain elusive, with no consensus on the most effective approaches [5].

Various clinical imaging techniques, including ultrasound, computed tomography (CT), and magnetic resonance imaging (MRI), have been employed to explore the underlying classification and mechanisms of cLBP. CT provides high-resolution cross-sectional images, offering detailed visualization of various anatomical structures, including the vertebrae and muscles [6-8]. However, CT imaging exposes patients to ionizing radiation, which carries potential long-term health risks. Also, it has limited ability to differentiate between

soft tissues, making it less effective for detailed assessment of muscular structures [9]. MRI is a non-invasive diagnostic tool that uses powerful magnetic fields and radio waves to produce high-resolution images, particularly suited for visualizing soft tissues, organs, and nervous systems [10, 11]. However, MRI imaging is generally more expensive, less accessible, and time-consuming compared to other imaging methods, limiting its use. By comparison, ultrasound imaging offers a cost- and time-effective alternative without the risks associated with ionizing radiation, making it a valuable and widely used tool in clinical practice for assessing cLBP.

Current ultrasound research on cLBP employs predominantly two-dimensional (2-D) ultrasound imaging to assess muscle thickness, contraction, and tissue echogenicity, which are believed to be associated with LBP[12]. This 2-D imaging approach overlooks volumetric and intricate anatomical structures and thus limits the comprehensiveness of the analysis [13]. In contrast, three-dimensional (3-D) ultrasound imaging offers improved spatial visualization, enabling a more detailed and accurate layer-by-layer analysis from the dermis to the muscle. This comprehensive volumetric data allows for the identification of subtle morphological changes and the assessment of tissue interactions, making 3-D ultrasound a superior modality for studying cLBP. However, each 3-D scan can produce hundreds of image slices, making manual annotation extremely labor-intensive and limiting the availability of annotated data necessary for training robust deep learning models. Also, this technique may be constrained by limited penetration depth and is prone to artifacts and noise, which can compromise image quality[14]. Furthermore, existing studies typically focus on a limited number of tissues rather than performing a comprehensive layer-by-layer analysis from the dermis to the muscle. Consequently, essential information regarding individual tissues and their interactions across layers might be omitted. Therefore, an automated layer-by-layer segmentation solution would be highly valuable for identifying image biomarkers associated with cLBP from 3-D ultrasound imaging data.

To address the challenge of training AI models with limited annotated data, several advanced machine learning techniques are being explored, including sample-efficient learning (SEL) and Semi-supervised learning (SSL)[15]. SEL aims to maximize model performance while minimizing training samples. Common SEL strategies include synthesizing samples with image transformation [16], GAN model [17], diffusion model [18], or image registration model [19]. However, studies have shown that the degree of augmentation must be carefully

calibrated and both over-augmentation and under-augmentation can hinder model performance [20]. A promising approach is to guide augmentation using feedback from downstream task losses, thereby eliminating the need to predefine an optimal augmentation policy. For example, smart augmentation creates composite images tailored to minimize downstream model losses and improve model learning [21]. In contrast, AdvChain introduced adversarial augmentation, where the augmentation model is trained to maximize the downstream model loss and generate more challenging and diverse samples [22]. While these two studies appear contradictory, a recent survey on curriculum learning (CL) indicates both easy and hard samples can be valuable for effective training [23], and easy samples speeds up convergence at early training stage [24]. Unfortunately, none of the existing augmentation methods focus on generating easy-to-learn samples. SSL complements SEL by leveraging a small amount of labeled data along with a larger pool of unlabeled data to improve model performance and generalization [15, 25-29]. Despite its promise, SSL relies heavily on high-quality labeled data and key assumptions, such as smoothness (similar inputs yield similar predictions) and clustering (data naturally forms distinct groups), which may not always hold in real-world settings.

In this study, we propose an innovative framework termed generative reinforcement network (GRN). GRN integrates generative and segmentation models (segmentor) through a collaborative learning loop. Unlike traditional data augmentation techniques, GRN establishes a feedback mechanism where the segmentation model actively guides the generator during each training iteration via back-propagated losses. This design ensures that the generator produces easy-to-learn augmented images specifically optimized to improve segmentation performance. Additionally, interpolation consistency training is employed to generate challenging samples to enhance the model’s robustness when applied to unseen data. During inference, the generator also functions as an image enhancement tool for preprocessing inputs by emphasizing features critical for segmentation, thereby improving the reliability of tissue segmentation. GRN supports both SEL and SSL scenarios. By reducing the dependence on extensive manual labeling, it achieves competitive and often superior performance compared to fully supervised models. This efficiency makes GRN particularly effective for problems like ours, namely tissue layer segmentation in 3-D ultrasound imaging.

II. MATERIALS AND METHODS

A. Study Dataset

The dataset is acquired from an ongoing project funded by the National Institute of Health (NIH), which enrolls participants with cLBP and healthy controls (Institutional Review Board: STUDY22090014). All participants were positioned face-down on an examination table. The ultrasound array transducer was placed laterally to the midline at the lumbar 3-4 (L3-L4) vertebral interspace (Fig. 1, Part 1), specifically targeting the multifidus (MF) and erector spinae (ES) muscles. A row-column array (RCA) transducer (RC6gV, Vermon), operating at a center frequency of 6 MHz with an active aperture of 25.6

mm \times 25.6 mm, was connected to the Vantage 256 ultrasound system (Verasonics Inc., WA, USA) to acquire 3-D volumetric ultrasound data. A synthetic aperture technique was used during acquisition to improve image quality. To acquire a single frame, each element of the transducer individually transmits one pulse in sequence until all the elements have performed transmissions, and after each transmission, all the elements simultaneously receive the echo signals. This enabled a synthetic aperture (SA) approach to achieve dynamic focusing during beamforming for image reconstruction.

Temporal compounding was applied by averaging three consecutive frames to improve the image signal-to-noise ratio. Both the right and left sides of the back were scanned. On each side, two specific locations over the MF and ES muscles were targeted by experienced ultrasound examiners (Drs. Wasan and Bean). Each designated location was scanned three times, yielding a total of twelve B-mode scans per participant. A total of 29 participants were enrolled and used for this study. We randomly sampled 69 scans ($N_{image} = 17,664$) taken from various locations across 29 patients for algorithm development (Table I). An experienced ultrasound operator (Ms. Zhao) meticulously annotated six distinct anatomical layers depicted on the 3-D ultrasound scans, including the dermis, superficial fat, superficial fascial membrane (SFM), deep fat, deep fascial membrane (DFM), and MF muscle (Figure 1, Parts 2 & 3). The annotated images were divided into training ($N_{image} = 10,722, N_{scan} = 44, N_{patient} = 16$), internal validation ($N_{image} = 512, N_{scan} = 2, N_{patient} = 2$), and independent test ($N_{image} = 6,430, N_{scan} = 23, N_{patient} = 11$) sets at the patient level. To ensure a more reliable estimate of model performance, we set aside a relatively larger testing set comprising 23 scans from different patients’ locations.

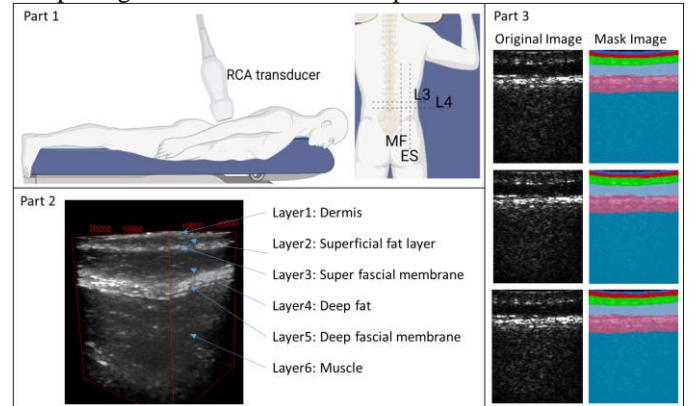


Fig. 1. 3-D ultrasound B-mode image acquisition and annotations. Part 1: ultrasound image acquisition. Part 2: A 3-D ultrasound B-mode image depicting six tissue layers. Part 3: Original B-mode images along the coronal or sagittal directions paired with their corresponding annotations, where each color represents a specific tissue layer.

TABLE I
DESCRIPTIVE STATISTICS INFORMATION FOR DEMOGRAPHIC VARIABLES AND LBP STATUS

	N = 29	Summary
Demographic variable		
Age		47.11(19.34)
Female		18(62.07%)
Hispanic or Latino		1(3.44%)
African American		2(6.90%)
Non-hispanic White		26(89.65%)

Height (in inches)	66.38(3.80)
Weight(in pounds)	179.83(36.02)
LBP status	
Positive	21(72.41%)

Summary statistics are reported as mean (standard deviation) for continuous measurements and percentages for categorical measurements.

B. Generative Reinforcement Network

Inspired by CL’s insights that both easy and challenging data drive better training [30], GRN is designed to generate both challenging interpolated samples and easy-to-learn samples to improve segmentation model performance (Fig. 2.). Within this framework, we introduce two variants: **GRN-SEL** for sample-efficient learning and **GRN-SSL** for semi-supervised learning. In GRN-SEL, the generator G reconstructs the original image, which is then passed through the segmentor. We utilize a feedback mechanism where the segmentor provides feedback to the generator via the segmentor loss during each training iteration. This feedback mechanism allows the generator to create easy-to-learn reconstructed images that minimize segmentor loss for faster model convergence. This approach, termed **reinforcement augmentation (RAug)**, optimizes the following objective function:

$$\min_G \left(\min_S L_{seg}(S(G(x)), y) \right), \text{ where } x \sim p_{data}(x) \quad (1)$$

where x is sampled from the prior distribution $p_{data}(x)$, and y represents the ground truth. G and S denote the generator and segmentor, respectively. L_{seg} is the segmentor’s loss. To better capture complex patterns, GRN-SSL incorporates interpolation consistency training, which generates challenging interpolated samples.

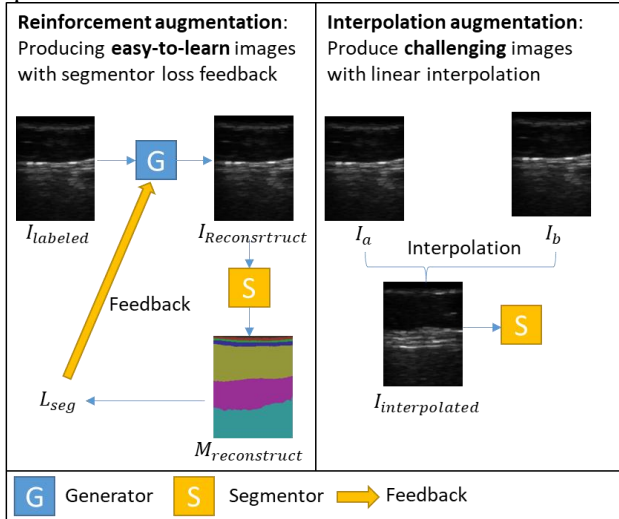


Fig. 2. Illustration of GRN-based data augmentation. RAug creates easy-to-learn images to help the model quickly learn simple patterns, while interpolation augmentation provides challenging samples to learn complex patterns.

1) Sample-efficient and Semi-supervised Generative Reinforcement Network

GRN-SEL combines a GAN model with the segmentor feedback mechanism (Fig. 3). In each training iteration, the generator G_θ processes each labeled image to produce a reconstructed version. The segmentor $S_{\theta'}$ then generated predicted masks from those reconstructed images. A Dice loss is calculated based on the difference between these predicted masks and the ground truth masks, and the loss is back-

propagated to the generator. This feedback encourages G_θ to improve its reconstruction by minimizing the segmentor loss, which assist model convergence and helps it learn simple pattern, especially when training data are scarce.

Like a traditional GAN model, the generator G_θ also receives feedback from the discriminator $D_{\theta'}$, which classifies each reconstructed image as real or fake. Additionally, the segmentor processes both original, unaltered images and the reconstructed images and calculates a combined Dice loss based on mask prediction from both. This dual-processing approach promotes the segmentation model’s robustness and stability by ensuring consistent performance on both generator-processed and original images. The comprehensive loss functions are defined as follows:

$$L_G = \lambda_{adv} L_{MSE}(D_{\theta'}(\hat{I}_L), 1) + \lambda_{seg} L_{Dice}(\hat{M}_L, M) + \lambda_{L1} L1(\hat{I}_L, I_L) \quad (2)$$

$$L_S = \frac{L_{Dice}(M_L, M) + L_{Dice}(\hat{M}_L, M)}{2} \quad (3)$$

$$L_D = \frac{L_{MSE}(D_{\theta'}(I_L), 1) + L_{MSE}(D_{\theta'}(\hat{I}_L), 0)}{2} \quad (4)$$

// 1: Real, 0: Fake

where L_{MSE} represents the Mean Squared Error (MSE) loss. L_{Dice} represents the Dice loss and $L1$ represents the L1 loss. λ_{adv} , weights λ_{seg} and λ_{L1} control the contributions to each loss component. I_L and \hat{I}_L are the labeled image and its reconstructed version. M is the ground truth mask. M_L and \hat{M}_L are the mask predictions for the labeled image and reconstructed image, respectively. The generator loss function combines both generator and discriminator feedback loss terms, ensuring image generation supports not only realism but also effective learning by the segmentor.

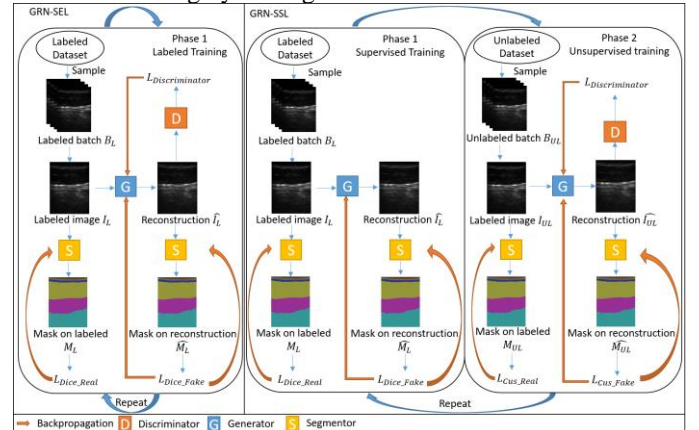


Fig. 3. Architectures of GRN-SEL and GRN-SSL. In GRN-SEL the generator receives feedback from the segmentor through backpropagation of the segmentation loss L_{Dice_Fake} . GRN-SSL operates in two phases: Phase 1 (supervised training) and phase 2 (unsupervised training) with batches of equal size sampled from each dataset to ensure balanced contributions from labeled data and unlabeled data. The GRN-SSL architecture is similar to that of GRN-SEL, except that during the unsupervised training phase, a customized loss that evaluates model prediction on unlabeled images is backpropagated to the generator.

GRN-SSL extends the segmentor feedback mechanism to the unlabeled training process by replacing the segmentation loss with a customized loss that evaluates segmentation model consistency (i.e., interpolation consistency loss in this study)

(Fig. 3). A two-phase alternate-batch strategy is implemented to balance labeled and unlabeled datasets. In each iteration, a labeled B_L and an unlabeled batch B_{UL} are sampled from the labeled dataset $Dataset_L(I, M)$ and the unlabeled dataset $Dataset_{UL}(I, M)$, respectively. The training process includes two phases for each iteration, a supervised training phase with B_L and an unsupervised training phase with B_{UL} . The supervised training phase mirrors the process in GRN-SEL, except that discriminator training is moved to the unsupervised training phase. Since $Dataset_{UL}(I, M)$ contains significantly more images than $Dataset_L(I, M)$, including the discriminator in the unsupervised training is sufficient to enhance model robustness. The loss functions are as follows:

$$L_G = \lambda_{seg} L_{Dice}(\widehat{M}_L, M) + \lambda_{L1} L1(\widehat{I}_L, I_L) \quad (5)$$

$$L_S = \frac{L_{Dice}(M_L, M) + L_{Dice}(\widehat{M}_L, M)}{2} \quad (6)$$

In the unsupervised training phase, the generator processes unlabeled images to produce reconstructed versions, and the segmentor generates the corresponding masks. Instead of using traditional segmentation loss like GRN-SEL, a customized consistency loss $L_{customize}$ is defined and back-propagated to the generator. The customized consistency loss can be any predefined loss function used to evaluate model robustness. In this study, we specifically use interpolation consistency loss. As in GRN-SEL, the discriminator evaluates the realism of the generated images and provides feedback to guide image generation. The overall loss function for phase 2 is defined as follows:

$$L_G = \lambda_{adv} L_{MSE}(D_{\theta'}(\widehat{I}_{UL}), 1) + \lambda_{cus} L_{customize}(\widehat{M}_{UL}, M) + \lambda_{L1} L1(\widehat{I}_{UL}, I_{UL}) \quad (7)$$

$$L_S = \frac{L_{customize}(\widehat{M}_{UL}) + L_{customize}(M_{UL})}{2} \quad (8)$$

$$L_D = \frac{L_{MSE}(D_{\theta'}(I_{UL}), 1) + L_{MSE}(D_{\theta'}(\widehat{I}_{UL}), 0)}{2} // 1: Real, 0: Fake \quad (9)$$

where I_{UL} and \widehat{I}_{UL} represent the unlabeled image and its reconstructed version, respectively M is the ground truth mask. M_{UL} and \widehat{M}_{UL} denote the mask predictions for the unlabeled image and the reconstructed unlabeled image, respectively.

Note that the gradients of L_{Dice} in GRN-SEL and $L_{customize}$ in GRN-SSL are passed through generator G and segmentor S simultaneously to enable mutual influence and enhance each other's performance during each training iteration.

Algorithm 1 The Generative Reinforcement Network (GRN) Algorithm for sample-efficient learning

Require: G_θ : Generator with trainable parameters θ
Require: $D_{\theta'}$: Discriminator with trainable parameters θ'
Require: $S_{\theta''}$: Segmentor with trainable parameters θ''
Require: $Dataset_L(I, M)$: Collection of labeled samples
Require: T : total number of iterations

```

for t = 1, ..., T do
  Sample  $I_L, M \sim Dataset_L(I, M)$ 
   $\widehat{I}_L = G_\theta(I_L)$ 
   $P_L = D_{\theta'}(I_L)$ 
   $\widehat{P}_L = D_{\theta'}(\widehat{I}_L)$ 
   $L_D = (L_{MSE}(P_L, 1) + L_{MSE}(\widehat{P}_L, 0))/2 // 1: Real, 0: Fake$ 
  Update  $\theta'$  based on  $L_D$ 
   $\widehat{M}_L = S_{\theta''}(\widehat{I}_L)$ 

```

```

   $L_G = \lambda_{adv} L_{MSE}(\widehat{P}_L, 1) + \lambda_{seg} L_{Dice}(\widehat{M}_L, M_L) + \lambda_{L1} L1(\widehat{I}_L, I_L)$ 
  // 1: Real, 0: Fake
  Update  $\theta$  based on  $L_G$ 
   $M_L = S_{\theta''}(I_L)$ 
   $L_S = (L_{Dice}(M_L, M) + L_{Dice}(\widehat{M}_L, M))/2$ 
  Update  $\theta''$  based on  $L_S$ 
end for
return  $\theta, \theta', \theta''$ 

```

Algorithm 2 The Generative Reinforcement Network (GRN) Algorithm for semi-supervised learning

Require: G_θ : Generator with trainable parameters θ
Require: $D_{\theta'}$: Discriminator with trainable parameters θ'
Require: $S_{\theta''}$: Discriminator with trainable parameters θ''
Require: $Dataset_L(I, M)$: Collection of labeled samples
Require: $Dataset_{UL}(I, M)$: Collection of labeled samples
Require: T : total number of iterations

```

for t = 1, ..., T do
  Sample  $I_L, M \sim Dataset_L(I, M)$ 
   $\widehat{I}_L = G_\theta(I_L)$ 
   $\widehat{M}_L = S_{\theta''}(\widehat{I}_L)$ 
   $L_G = \lambda_{seg} L_{Dice}(\widehat{M}_L, M) + \lambda_{L1} L1(\widehat{I}_L, I_L)$ 
  Update  $\theta$  based on  $L_G$ 
   $M_L = S_{\theta''}(I_L)$ 
   $L_S = (L_{Dice}(M_L, M) + L_{Dice}(\widehat{M}_L, M))/2$ 
  Update  $\theta''$  based on  $L_S$ 
  Sample  $I_{UL} \sim Dataset_{UL}(I, M)$ 
   $\widehat{I}_{UL} = G_\theta(I_{UL})$ 
   $P_L = D_{\theta'}(I_{UL})$ 
   $\widehat{P}_L = D_{\theta'}(\widehat{I}_{UL})$ 
   $L_D = (L_{MSE}(P_L, 1) + L_{MSE}(\widehat{P}_L, 0))/2 // 1: Real, 0: Fake$ 
  Update  $\theta'$  based on  $L_D$ 
   $\widehat{M}_{UL} = S_{\theta''}(\widehat{I}_{UL})$ 
   $L_G = \lambda_{adv} L_{MSE}(\widehat{P}_L, 1) + \lambda_{cus} L_{customize}(\widehat{M}_{UL}) + \lambda_{L1} L1(\widehat{I}_{UL}, I_{UL}) // 1: Real, 0: Fake$ 
  Update  $\theta$  based on  $L_G$ 
   $M_{UL} = S_{\theta''}(I_{UL})$ 
   $L_S = (L_{customize}(\widehat{M}_{UL}) + L_{customize}(M_{UL}))/2$ 
  Update  $\theta''$  based on  $L_S$ 
end for
return  $\theta, \theta', \theta''$ 

```

2) Segmentation Guided Enhancement (SGE)

In the GRN framework, the objective function is defined as $\min_G \min_S L_{seg}(S(G(x)), y)$, where the generator G and the segmentor S share the same goal to minimize the segmentor loss. Consequently, during the inference phase, the generator and the segmentor can be integrated to provide a joint prediction $y = S(G(x))$. This two-step process, termed Segmentation Guided Enhancement (SGE), ensures that image enhancements are directly designed to improve segmentation outcomes.

C. Interpolation Consistency Loss

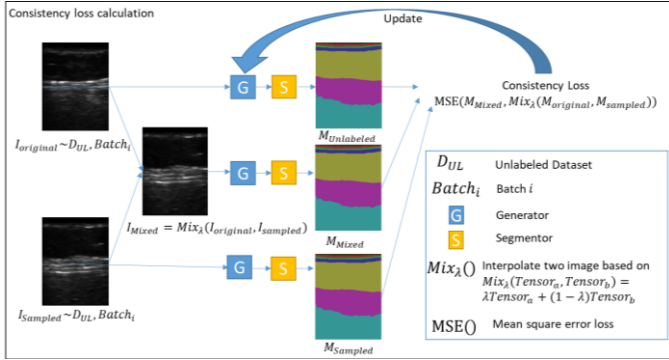


Fig. 4. Interpolation Consistency Loss Calculation. I_{UL} represents the unlabeled image, and I_S denotes a randomly sampled image from the same batch. The interpolation consistency loss enforces the model to ensure that the predicted mask from the mixed image I_M closely aligns with the interpolated mask derived from the unlabeled image I_{UL} and the randomly sampled image I_S .

Similar to a previous study [31], we adopt interpolation consistency loss as our customized loss for GRN-SSL. For each image in the unlabeled batch B_{UL} , we randomly sample a second image from the same batch. Both images are processed by the generator G and segmentor S to produce their respective segmentation masks. We then randomly generate an interpolation coefficient λ from a predefined distribution to create a mixed image through an interpolation of the original and sampled images. This mixed image is subsequently processed by the generator and segmentor to obtain a corresponding segmentation mask. The interpolation consistency loss quantifies the alignment between the segmentation mask of the mixed image and the interpolated masks of the original and sampled images.

$$L_{ICT} = MSE(M_{mixed}, Mix_{\lambda}(M_{UL}, M_S)) \quad (12)$$

where M_{mixed} denotes the predicted mask derived from the mixed image. M_{UL} and M_S are the mask predictions based on the unlabeled image and randomly sampled image, respectively. $Mix_{\lambda}()$ performs the interpolation of two images based on $Mix_{\lambda}(Tensor_a, Tensor_b) = \lambda Tensor_a + (1 - \lambda) Tensor_b$.

D. Backbone Network Architecture

The backbone segmentation network utilizes a 2D Unet model configured with encoder channels of (16, 32, 64, 128, 256). The model is designed to accept single-channel input and produce segmentation masks for 7 classes, making it well-suited for our ultrasound imaging segmentation task. The generator encoder, illustrated in the upper section of Fig 5, incorporates residual blocks to improve gradient flow efficiency and facilitate the training of deeper network layers. The encoding process begins with an initial convolution layer that reduces spatial dimensions while increasing feature depth. This is followed by a series of residual blocks that downsample the input data. In contrast, the decoder utilizes 2D transposed convolutions to upscale high-dimensional feature representations, effectively reconstructing the images. Similar to the pix2pix model [32], we utilize a PatchGAN discriminator to assess the realism of generated images at the patch level [32]. The discriminator architecture comprises several convolution layers that progressively extract features from the input images.

The discriminator outputs a patch-wise label map that evaluates the authenticity of each patch on the image.

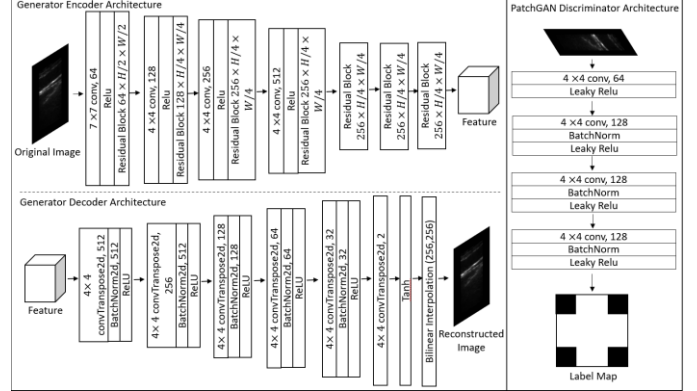


Fig. 5. Backbone network architecture. The encoder (upper section, left) utilizes multiple residual blocks to progressively capture high-dimensional patterns. The decoder (lower section, left) reconstructs the image-mask pairs (IMPs) from these high-level representations using transposed convolution layers, facilitating the accurate generation of segmentation masks.

E. Model Training and Performance Evaluation

In line with standard practices in SSL and SEL, we designated 5%, 10%, and 20% of the training dataset at the patient level as labeled subsets, with the remaining data serving as an unlabeled subset, for an initial comparison of GRN methods against existing approaches. We compared the performance of GRN variants with that seven other SSL methods, including MT[25], UAMT [26], Uncertainty Rectified Pyramid Consistency (URPC) [33], Shape-aware Semi-supervised network (SASSNet) [34], Regularized dropout (R-drop) [35], Interpolation Consistency Training (ICT) [31], and Deep Adversarial Network (DAN) [36]. All SSL methods, including our GRN variants and seven other comparison methods, utilized the UNet model as their backbone network.

To benchmark the GRN methods against a fully supervised setting, where the model is trained on all labeled images, we allocated 30%, 40%, 50%, and 100% of the training dataset as labeled for comparison. This approach allows the evaluation of the effectiveness of GRN methods in reducing the need for extensive image annotation while maintaining and even enhancing segmentation performance.

We analyzed the effect of RAug, SGE, and SSL on model performance across varying proportions of labeled images for training. The effect of RAug was assessed by calculating the difference in dice similarity coefficient (DSC) between the GRN-SEL method and the fully supervised model. The effect of SGE effect was determined by comparing GRN variants with and without SGE, while the effect of SSL was evaluated by measuring the performance difference with or without the inclusion of unlabeled data for unsupervised training. Additionally, we conducted an ablation study on a 5% labeled dataset to evaluate the GRN model performance.

In training the GRN-SEL, λ_{adv} , λ_{seg} and λ_{L1} in L_G are set to 1, 100, 100, respectively. For GRN-SSL training, λ_{seg} and λ_{L1} are both set to 100. In the unsupervised training of GRN-SSL, λ_{adv} , $\lambda_{customize}$ and λ_{L1} are set to be 1, 1, 100, respectively. Following the approach of the pix2pix model [32], a smaller weight was assigned to the adversarial loss. The Adam optimizer was used for training the generator, segmentor, and

discriminator, with an initial learning rate of 0.0002 and exponential decay rates β set to be (0.5, 0.999). The maximum number of epochs was set to 50. The model with the lowest dice loss on the validation dataset was selected. An early stopping mechanism was implemented, terminating the training if validation performance did not improve for five consecutive epochs. The performance of the segmentation model was evaluated based on the DSC on the independent test sets, with a higher DSC indicating a greater overlap between the predicted mask and the ground truth mask. In this study, all methods were implemented using PyTorch = 2.3.1 on an NVIDIA GTX3090 GPU.

III. RESULTS

A. Performance Evaluation and Comparison

Table II presents the segmentation performance of our proposed GRN methods compared to existing techniques on the independent test set with varying proportions of labeled data (5%, 10%, 20%) involved in the training. Across all labeled data proportions, the GRN-SSL variant and GRN-SEL with SGE consistently outperformed other methods. When trained on 5% labeled data, GRN-SEL achieved superior results compared to 5 out of 7 models without utilizing unlabeled images. At the 10% labeled level, GRN-SSL (w SGE) is only 3.46% lower than the fully supervised model trained on all labeled data. At the 20% labeled level, GRN-SSL with SGE achieved an 80.05% DSC, which is just 0.57% lower than the fully supervised model (80.62%); however, this difference is still statistically significant ($p < 0.05$).

Table III summarizes the mean DSC for each tissue layer as well as the overall mean when trained on 5% of the labeled images in the training set. The GRN-SSL variant with SGE outperformed all other methods in 3 out of 6 tissue layers significantly, while GRN-SSL exceeded the performance of other methods in 2 out of 6 layers. Although the overall DSC for GRN-SEL with SGE was higher, it did not achieve a statistically significant improvement in the segmentation of individual layers. Some examples in Fig. 6 show the prediction results of the GRN methods and other models.

TABLE II

COMPARISON OF SEGMENTATION PERFORMANCE BETWEEN OUR METHODS AND EXISTING METHODS IN TERMS OF DICE COEFFICIENT (STANDARD DEVIATION)

Method	Labeled %		
	5%	10%	20%
Fully supervised	43.97±0.26	64.87±0.30	74.52±0.29
MT[25]	65.09±0.31	72.78±0.31	76.82±0.25

TABLE III

COMPARISON OF SEGMENTATION PERFORMANCE FOR EACH TISSUE LAYER AMONG GRN METHODS AND OTHER MODELS TRAINED ON THE 5% LABELED IMAGES IN THE TRAINING DATASET, EXPRESSED BY DICE COEFFICIENT (STANDARD DEVIATION)

Methods	Dermis	Superficial Fat Layer	SFM	Deep Fat	DFM	Muscle	Overall
Fully supervised	7.06±0.19	0.67±0.03	57.69±0.30	63.76±0.75	65.78±0.44	68.89±0.32	43.97±0.26
MT	62.98±0.32	59.81±0.41	69.45±0.39	62.41±0.74	66.40±0.42	69.49±0.35	65.09±0.31
UAMT	60.18±0.38	52.43±0.50	71.09±0.46	63.06±0.75	69.14±0.43	70.44±0.34	64.39±0.35
URPC	46.78±0.64	18.71±0.38	64.96±0.61	66.90±0.79	67.03±0.44	74.36±0.39	56.46±0.29
SASSNet	34.33±0.64	27.29±0.61	58.28±0.53	68.30±0.76	60.13±0.48	67.62±0.31	52.66±0.28
R-drop	65.05±0.30	55.16±0.51	68.70±0.40	67.18±0.72	66.65±0.43	72.32±0.30	65.92±0.33
ICT	65.91±0.28	55.44±0.47	70.25±0.42	64.40±0.71	68.68±0.42	71.75±0.28	66.07±0.32
DAN	62.59±0.29	46.79±0.34	73.93±0.25	63.77±0.68	67.95±0.45	72.35±0.27	64.56±0.26
GRN-SEL	63.58±0.38	54.87±0.48	69.83±0.39	63.90±0.73	68.28±0.43	70.47±0.43	65.16±0.34
GRN-SEL (w SGE)	65.15±0.39	56.73±0.48	71.23±0.41	65.83±0.77	68.61±0.45	71.70±0.33	66.55±0.34

UAMT[26]	64.39±0.35	72.75±0.33	76.95±0.26
URPC[33]	56.46±0.29	73.62±0.19	76.94±0.18
SASSNet[34]	52.66±0.28	67.27±0.25	76.49±0.20
R-drop[35]	65.92±0.35	75.34±0.26	77.35±0.36
ICT[31]	66.07±0.32	74.06±0.25	76.54±0.22
DAN[36]	64.56±0.26	73.00±0.27	74.34±0.26
GRN-SEL	65.16±0.34	73.08±0.28	75.72±0.27
GRN-SEL (w SGE)	66.55±0.34	76.98±0.26	78.85±0.25
GRN-SSL	67.33±0.30	75.65±0.28	77.61±0.34
GRN-SSL (w SGE)	68.90±0.28	77.16±0.30	80.05±0.24

Bold denotes the proposed methods that significantly outperform all other methods ($p < 0.05$, paired t-test).

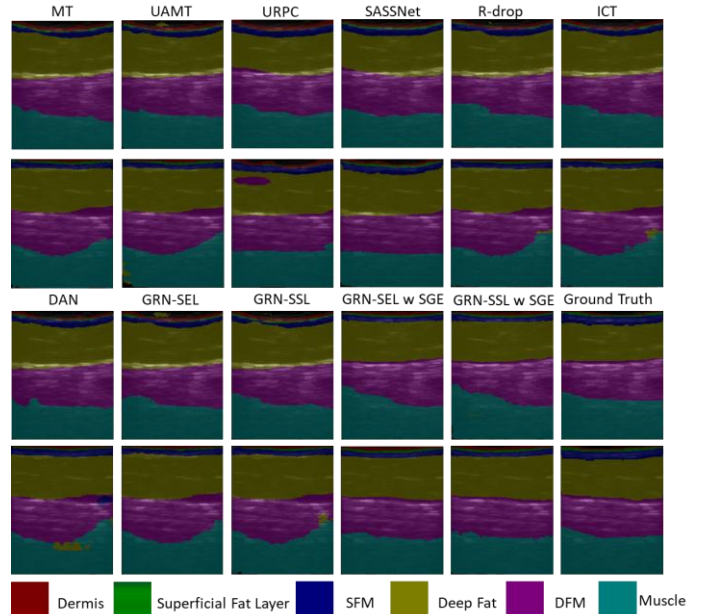


Fig. 6. Mask predictions for GRN methods and other methods when trained on the 5% labeled images in the training set. GRN variants, particularly those utilizing SGE, demonstrate superior segmentation performance and higher accuracy in tissue layer segmentation.

B. Segmentation Performance across Varying Proportions of Labeled Dataset

Table 4 presents the segmentation performance of GRN variants on varying proportions of labeled images in the training set. The results indicate that with just 30% of the labeled images, the GRN-SEL with SGE achieved performance comparable to the model trained on 100% of the labeled images. Additionally, when utilizing 30% of the labeled dataset, the GRN-SSL with SGE attained performance statistically similar

GRN-SSL	67.06±0.29	58.88±0.42	68.85±0.44	67.46±0.70	67.14±0.41	74.57±0.41	67.33±0.30
GRN-SSL (w SGE)	69.40±0.29	61.91±0.38	72.11±0.42	68.15±0.71	67.17±0.37	74.63±0.28	68.90±0.28

Bold text denotes the proposed methods that statistically outperform all other methods. ($p < 0.05$, paired t-test).

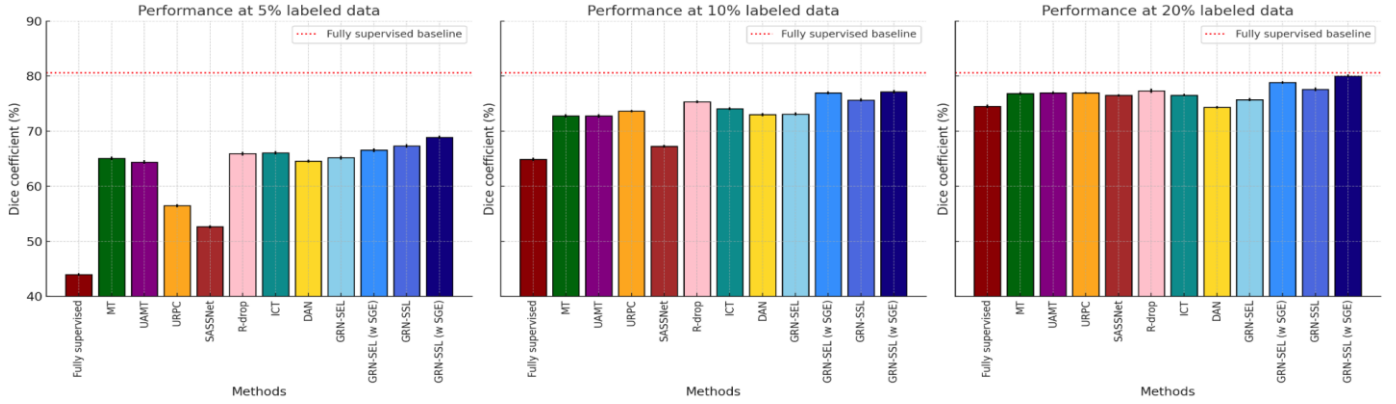


Fig. 7. Comparison of segmentation model performance across various methods trained on different amounts of labeled data (5%, 10%, and 20%). The red dotted line indicates the performance of the model when trained on 100% labeled images in the training set. The small bars on each column indicate the confidence intervals (CI) for the segmentation results of each method.

to the model trained on all labeled images. As the labeled image proportion increased to 40%, the GRN-SSL model matched the performance of the fully supervised approach. Even without utilizing the unlabeled dataset, the GRN-SEL achieved performance similar to those of the supervised model. Notably, the GRN framework not only maintained equivalence with fully supervised models under reduced labeling conditions but also exceeded their performance limits. Specifically, the GRN-SSL with SGE achieved a Dice coefficient that was 2.59% higher than that of the fully supervised model while utilizing only 40% of the labeled images in the training set. These findings suggest the efficacy of the GRN methods in enhancing segmentation performance while significantly reducing the need for extensive data labeling.

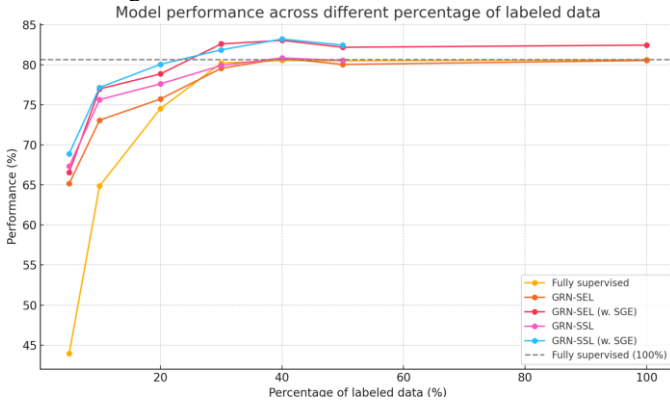


Fig. 8. Segmentation performance of GRN variants relative to the proportion of the labeled images in the training set. The dotted line indicates the performance of the models trained on all labeled images.

C. GRN Component Evaluation

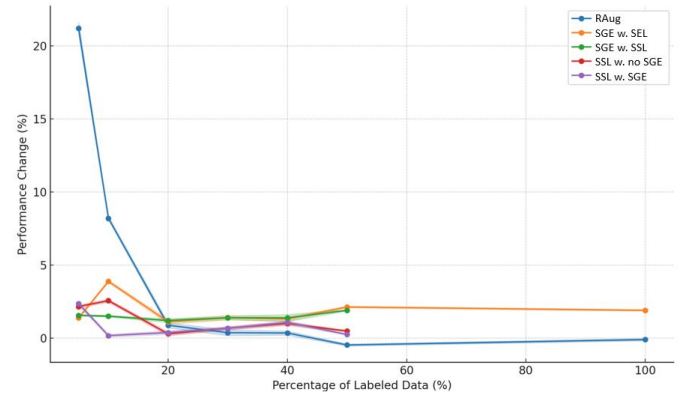


Fig. 9. Model performance with different GRN components across varying percentages of labeled images. The RAug significantly enhances performance at lower percentages of data images but shows a diminishing effect as more labeled data is incorporated. In contrast, SSL consistently shows a strong positive impact across most data proportions.

Table V presents the individual and combined effects of RAug, SGE, and SSL on model performance across different proportions (5%, 10%, 20%, 30%, 40%, 50%, and 100%) of labeled images in the training set. The results indicate that RAug has a substantial positive impact on model performance, particularly when the labeled data is scarce. Specifically, at lower labeling proportions (5% and 10%), RAug contributes to substantial performance gains of +21.19% and +8.21%, respectively. However, its positive impact diminishes as the number of labeled images increases, with the effect dropping to

TABLE IV

COMPARISON OF SEGMENTATION PERFORMANCE FOR EACH TISSUE LAYER AMONG GRN METHODS AND OTHER MODELS TRAINED ON THE 5% LABELED IMAGES IN THE TRAINING DATASET, EXPRESSED IN TERMS OF DICE COEFFICIENT (STANDARD DEVIATION)

Method	5%	10%	20%	30%	40%	50%	100%
Fully supervised	43.97±0.26	64.87±0.30	74.52±0.29	80.21±0.17	80.53±0.17	80.49±0.16	80.62±0.15
GRN-SEL	65.16±0.34	73.08±0.28	75.72±0.27	79.55±0.17	80.79±0.15	80.04±0.14	80.53±0.14
GRN-SEL (w. SGE)	66.55±0.34	76.98±0.26	78.85±0.25	82.60±0.15	83.04±0.14	82.18±0.14	82.45±0.12
GRN-SSL	67.33±0.30	75.65±0.28	77.61±0.34	79.90±0.17	80.85±0.15	80.53±0.14	-
GRN-SSL (w. SGE)	68.90±0.28	77.16±0.30	80.05±0.24	81.86±0.16	83.21±0.14	82.45±0.13	-

Bold text denotes the proposed methods statistically not inferior to 100% fully supervised model. ($p < 0.05$, paired t-test).

TABLE V

EFFECT OF DGA, SGE, AND SSL ON SEGMENTATION PERFORMANCE GAINS ACROSS VARIOUS PROPORTIONS OF LABELED IMAGES IN THE TRAINING SET, EXPRESSED IN TERMS OF DICE COEFFICIENT (STANDARD DEVIATION)

Variable	5%	10%	20%	30%	40%	50%	100%
DGA	+21.19±0.43	+8.21±0.12	+0.89±0.17	+0.38±0.20	+0.36±0.14	-0.46±0.07	-0.09±0.08
SGE w. SEL	+1.39±0.07	+3.89±0.08	+1.13±0.17	+1.41±0.15	+1.32±0.15	+2.14±0.06	+1.91±0.05
SGE w. SSL	+1.57±0.05	+1.51±0.06	+1.21±0.13	+1.40±0.12	+1.39±0.24	+1.91±0.05	
SSL w. no SGE	+2.17±0.10	+2.57±0.10	+0.30±0.13	+0.69±0.10	+1.01±0.13	+0.49±0.05	
SSL w. SGE	+2.36±0.12	+0.18±0.09	+0.39±0.12	+0.68±0.10	+1.08±0.12	+0.26±0.05	

Bold text denotes the proposed methods that statistically decrease the model performance. ($CI_{bounds} < 0$, $p < 0.05$, paired t-test).

-0.09% when all labeled images are used. In contrast, SGE consistently enhanced model performance across all proportions of labeled images, showing stable and robust improvements. The inclusion of SGE leads to positive effects ranging from +1.13% at 20% labeled images to +3.89% at 10%.

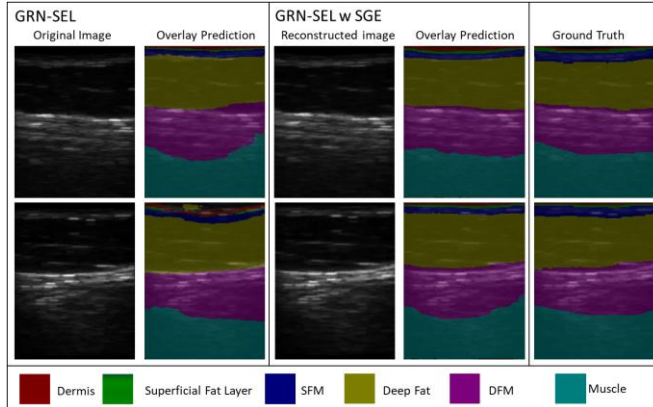


Fig. 10. Comparison of non-enhanced and enhanced images with corresponding mask prediction. The segmentation models achieve higher accuracy when utilizing SGE.

D. Ablation Study

TABLE VI

RESULTS OF THE ABLATION STUDY EVALUATING THE PROPOSED GRN FRAMEWORK ON THE VALIDATION DATASET WHEN 5% OF IMAGES BEING LABELED

Method	DSC(%)	Improvement(%)
Fully Supervised	40.02±0.53	-
Fully Supervised (w. image augmentation)	38.15±0.37	-1.87
Fully Supervised (w. GAN augmentation)	53.82±0.71	+13.80
GRN-SEL	57.12±0.93	+17.10
GRN-SEL (w. SGE)	57.30±0.86	+17.28
GRN-SEL (w/o L_{seg} feedback)	51.36±0.98	+11.34
GRN-SEL (Freeze S for back-propagate L_G)	48.56±1.11	+8.54
GRN-SSL (w. SGE)	65.10±0.75	+25.08

Segmentation performance is presented as percentage \pm half of CI. Segmentation performance is calculated excluding the background class. Image augmentation includes geometric augmentation and intensity augmentation. GAN augmentation indicates train GAN model for reconstructed purposes and implement the pre-trained generator to generate joint dataset ($D_{original}, D_{reconstructed}$) for the segmentor to trained with. L_{seg} feedback indicates including segmentation loss L_{seg} term in generator loss L_G .

Table VI presents the results of the ablation study on the GRN framework. The findings indicate that neither standard image augmentation nor traditional GAN augmentation methods achieved a DSC as high as GRN-SEL with DGA. The inclusion of SGE yielded a marginal increase of 0.18%. The removal of L_{seg} feedback from GRN-SEL led to a significant 5.76% decrease in DSC. Additionally, freezing the segmentor weights

during the backpropagation of the generator loss L_G caused a further 8.56% decline in DSC. Conversely, implementing interpolation consistency loss with unlabeled data in unsupervised training resulted in the greatest improvement, increasing DSC by 25.08%.

IV. DISCUSSION

We developed and validated a novel method called GRN, which synergistically integrates the joint training of a generator and a segmentor to accurately segment tissue layers depicted on B-model ultrasound imaging while significantly reducing the need for extensive image annotations. Unlike traditional unconstrained GAN-based data augmentation methods, our GRN framework features a feedback mechanism in which the segmentation model provides feedback loss to the generator, thereby guiding the image generation process to produce easy-to-learn segmentation-optimized images. Our results demonstrate that GRN-SSL with SGE can reduce data labeling efforts by up to 70% (Table IV). Meanwhile, GRN-SSL alone achieves a 60% reduction, GRN-SEL with SGE also reduces data labeling efforts by 70%, and GRN-SEL alone reduces by 60%, all while maintaining performance comparable to fully supervised models. Notably, GRN-SSL with SGE outperforms models trained on all labeled images, achieving a 2.59% higher DSC with only 40% of the labeled images in the training set. The effectiveness of the GRN framework in labeling reduction could save hundreds of hours in manual tissue-layer annotation, especially for 3D ultrasound images containing hundreds of slices of 2D images. Additionally, the precise layer segmentation produced by GRN enables more reliable tissue layer analysis in cLBP patients, supporting improved diagnostics and target therapy development.

The GRN framework offers several advantages. First, the RAUG generates augmented images specifically optimized to enhance downstream task model performance, enabling more efficient training, particularly when labeled data is limited (Fig. 9.). Second, the generator serves as an optional image enhancement tool, specifically optimized to generate images that minimize the segmentor's loss, thereby further enhancing segmentation performance. Third, the GRN framework exhibits significant versatility. Based on the GRN-SEL, the Dice loss used to measure the performance of the segmentor could be replaced by other loss functions, such as interpolation consistency loss for GRN-SSL or rectified pyramid consistent loss in the URPC model [31, 33]. Lastly, unlike other SSL approaches that typically require a large set of unlabeled images, GRN-SEL only relies on a small set of annotated data and supports SSL without special requirements for the number of unlabeled images.

Contrary to the common belief that data augmentation should prioritize generating challenging datasets to enhance model performance [22], our ablation study results (table VI) demonstrate that easy-to-learn augmented datasets can also lead to performance gains. This finding is particularly relevant when labeled data is scarce or during the early stages of model training, as the model initially focuses on learning simple patterns [23]. RAUG is designed to minimize downstream task loss and generate easier samples that help the model quickly capture these fundamental patterns and improve performance. However, as more labeled data becomes available, the model shifts its focus toward learning more complex patterns. In such cases, RAUG becomes less effective, and techniques like interpolation consistency training offer greater benefits for model performance (Fig. 9.).

We did not freeze segmentor weights during the backpropagation of the generator loss L_G . Although GRN shares a feedback mechanism similar to GANs by allowing the generator to receive guidance, the role of the discriminator and segmentor diverse in GRN differ from those in conventional GAN architectures. In GRN, the objective function is $\min_G \left(\min_S L_{seg}(S(G(x)), y) \right)$, where the generator G and segmentor S work together to minimize the segmentation loss. Additionally, during the inference stage, the generator can serve as an image enhancement module, preprocessing input images before they enter the segmentor. Therefore, we opted not to freeze the segmentor weights. This design allows both the generator G and segmentor S to adapt dynamically with each training iteration.

Our study has limitations. First, the dataset size is small due to the slow progress of patient recruitment and ongoing data collection. This limitation motivates us to develop novel solutions that minimize the need for a large dataset without spending significant time on manual annotations. To further address this concern, we set aside a relatively large independent test dataset consisting of 6430 images from 23 scans acquired on different locations of 11 subjects. Second, the RAUG does not improve the model performance when more labeled images are included for training. (Table V) This is attributed to the model's fast convergence on easy-to-learn samples, making additional easimages less impactful on performance. Our experiments demonstrate that RAUG is particularly effective when the sample size of the annotated training dataset is limited. Furthermore, the integration of SGE requires the generator to preprocess the image initially, leading to additional computational demands during the inference stage. However, SGE is an optional tool, providing users the flexibility to enhance model performance. Notably, both GRN-SEL and GRN-SSL prove their effectiveness without relying on SGE, with GRN-SSL outperforming other methods even in the absence of SGE. Despite these limitations, our experiments demonstrated the potential of the GRN in reducing the effort required for manual annotation.

V. CONCLUSION

We introduce a segmentation-aware joint training framework called GRN designed to segment tissue layers in 3-D B-mode

ultrasound images. This innovative approach incorporates a segmentation loss feedback mechanism that enables the generator to produce reconstructed images specifically optimized to enhance the performance of the segmentation model. Our model achieves a higher performance compared to models trained on 100% labeled datasets, all while reducing the data labeling efforts by 60%. As a SSL method, GRN-SEL relies on a small set of annotated data and can effectively utilize available unlabeled images, even when their quantity is limited.

REFERENCES

- [1] W. Li *et al.*, "Peripheral and central pathological mechanisms of chronic low back pain: a narrative review," *Journal of pain research*, pp. 1483-1494, 2021.
- [2] N. Akter, "Impact of low back pain on quality of life among elderly," Bangladesh Health Professions Institute, Faculty of Medicine, the University ..., 2020.
- [3] R. D. Meucci, A. G. Fassa, and N. M. X. Faria, "Prevalence of chronic low back pain: systematic review," *Revista de saude publica*, vol. 49, p. 73, 2015.
- [4] F. Balagué, A. F. Mannion, F. Pellisé, and C. Cedraschi, "Non-specific low back pain," *The lancet*, vol. 379, no. 9814, pp. 482-491, 2012.
- [5] J. R. Chapman *et al.*, "Evaluating common outcomes for measuring treatment success for chronic low back pain," *Spine*, vol. 36, pp. S54-S68, 2011.
- [6] K. Yokosuka *et al.*, "Computed tomographic epidurography in patients with low back pain and leg pain: a single-center observational study," *Diagnostics*, vol. 12, no. 5, p. 1267, 2022.
- [7] M. Kamaz, D. Kiresi, H. Oguz, D. Emlik, and F. Levendoglu, "CT measurement of trunk muscle areas in patients with chronic low back pain," *Diagnostic and interventional radiology*, vol. 13, no. 3, p. 144, 2007.
- [8] L. A. Danneels, G. Vanderstraeten, D. C. Cambier, E. E. Witvrouw, H. J. De Cuyper, and L. Danneels, "CT imaging of trunk muscles in chronic low back pain patients and healthy control subjects," *European spine journal*, vol. 9, pp. 266-272, 2000.
- [9] T. M. Buzug, "Computed tomography," in *Springer handbook of medical technology*: Springer, 2011, pp. 311-342.
- [10] G. Katti, S. A. Ara, and A. Shireen, "Magnetic resonance imaging (MRI)—A review," *International journal of dental clinics*, vol. 3, no. 1, pp. 65-70, 2011.
- [11] D. Chou *et al.*, "Degenerative magnetic resonance imaging changes in patients with chronic low back pain: a systematic review," *Spine*, vol. 36, no. 21 Suppl, pp. S43-S53, 2011.
- [12] W. K. Cheung, J. P. Y. Cheung, and W.-N. Lee, "Role of ultrasound in low back pain: A review," *Ultrasound in medicine & biology*, vol. 46, no. 6, pp. 1344-1358, 2020.
- [13] B. L. Partik *et al.*, "3D versus 2D ultrasound: accuracy of volume measurement in human cadaver kidneys," *Investigative radiology*, vol. 37, no. 9, pp. 489-495, 2002.
- [14] Q. Huang and Z. Zeng, "A review on real - time 3D ultrasound imaging technology," *BioMed research international*, vol. 2017, no. 1, p. 6027029, 2017.
- [15] K. Han *et al.*, "Deep semi-supervised learning for medical image segmentation: A review," *Expert Systems with Applications*, p. 123052, 2024.
- [16] K. Maharana, S. Mondal, and B. Nemade, "A review: Data pre-processing and data augmentation techniques," *Global Transitions Proceedings*, vol. 3, no. 1, pp. 91-99, 2022.
- [17] M. Frid-Adar, I. Diamant, E. Klang, M. Amitai, J. Goldberger, and H. Greenspan, "GAN-based synthetic medical image augmentation for increased CNN performance in liver lesion classification," *Neurocomputing*, vol. 321, pp. 321-331, 2018.
- [18] B. Trabucco, K. Doherty, M. Gurinas, and R. Salakhutdinov, "Effective data augmentation with diffusion models," *arXiv preprint arXiv:2302.07944*, 2023.
- [19] J. Nalepa *et al.*, "Data augmentation via image registration," in *2019 IEEE International Conference on Image Processing (ICIP)*, 2019: IEEE, pp. 4250-4254.

-
- [20] C. Shorten and T. M. Khoshgoftaar, "A survey on image data augmentation for deep learning," *Journal of big data*, vol. 6, no. 1, pp. 1-48, 2019.
- [21] J. Lemley, S. Bazrafkan, and P. Corcoran, "Smart augmentation learning an optimal data augmentation strategy," *Ieee Access*, vol. 5, pp. 5858-5869, 2017.
- [22] C. Chen *et al.*, "Enhancing MR image segmentation with realistic adversarial data augmentation," *Medical Image Analysis*, vol. 82, p. 102597, 2022.
- [23] X. Wang, Y. Chen, and W. Zhu, "A survey on curriculum learning," *IEEE transactions on pattern analysis and machine intelligence*, vol. 44, no. 9, pp. 4555-4576, 2021.
- [24] Y. Bengio, J. Louradour, R. Collobert, and J. Weston, "Curriculum learning," in *Proceedings of the 26th annual international conference on machine learning*, 2009, pp. 41-48.
- [25] A. Tarvainen and H. Valpola, "Mean teachers are better role models: Weight-averaged consistency targets improve semi-supervised deep learning results," *Advances in neural information processing systems*, vol. 30, 2017.
- [26] L. Yu, S. Wang, X. Li, C.-W. Fu, and P.-A. Heng, "Uncertainty-aware self-ensembling model for semi-supervised 3D left atrium segmentation," in *Medical image computing and computer assisted intervention—MICCAI 2019: 22nd international conference, Shenzhen, China, October 13–17, 2019, proceedings, part II 22*, 2019: Springer, pp. 605-613.
- [27] X. Luo, J. Chen, T. Song, and G. Wang, "Semi-supervised medical image segmentation through dual-task consistency," in *Proceedings of the AAAI conference on artificial intelligence*, 2021, vol. 35, no. 10, pp. 8801-8809.
- [28] K. Wang *et al.*, "Semi-supervised medical image segmentation via a tripled-uncertainty guided mean teacher model with contrastive learning," *Medical Image Analysis*, vol. 79, p. 102447, 2022.
- [29] J. Lyu, B. Sui, C. Wang, Q. Dou, and J. Qin, "Adaptive feature aggregation based multi-task learning for uncertainty-guided semi-supervised medical image segmentation," *Expert Systems with Applications*, vol. 232, p. 120836, 2023.
- [30] Y. Huang *et al.*, "Curricularface: adaptive curriculum learning loss for deep face recognition," in *proceedings of the IEEE/CVF conference on computer vision and pattern recognition*, 2020, pp. 5901-5910.
- [31] V. Verma *et al.*, "Interpolation consistency training for semi-supervised learning," *Neural Networks*, vol. 145, pp. 90-106, 2022.
- [32] P. Isola, J.-Y. Zhu, T. Zhou, and A. A. Efros, "Image-to-image translation with conditional adversarial networks," in *Proceedings of the IEEE conference on computer vision and pattern recognition*, 2017, pp. 1125-1134.
- [33] X. Luo *et al.*, "Semi-supervised medical image segmentation via uncertainty rectified pyramid consistency," *Medical Image Analysis*, vol. 80, p. 102517, 2022.
- [34] S. Li, C. Zhang, and X. He, "Shape-aware semi-supervised 3D semantic segmentation for medical images," in *Medical Image Computing and Computer Assisted Intervention—MICCAI 2020: 23rd International Conference, Lima, Peru, October 4–8, 2020, Proceedings, Part I 23*, 2020: Springer, pp. 552-561.
- [35] L. Wu *et al.*, "R-drop: Regularized dropout for neural networks," *Advances in Neural Information Processing Systems*, vol. 34, pp. 10890-10905, 2021.
- [36] Y. Zhang, L. Yang, J. Chen, M. Fredericksen, D. P. Hughes, and D. Z. Chen, "Deep adversarial networks for biomedical image segmentation utilizing unannotated images," in *Medical Image Computing and Computer Assisted Intervention—MICCAI 2017: 20th International Conference, Quebec City, QC, Canada, September 11-13, 2017, Proceedings, Part III 20*, 2017: Springer, pp. 408-416.